CHEMISTRY OF MATERIALS

pubs.acs.org/cm Article

Interstitial Lithium Doping in $BiVO_4$ Thin Film Photoanode for Enhanced Solar Water Splitting Activity

Chenyu Zhou, Zachary Sanders-Bellis, Tyler J. Smart, Wenrui Zhang, Lihua Zhang, Yuan Ping,* and Mingzhao Liu*

Cite This: *Chem. Mater.* 2020, 32, 6401−6409 Read Online

ACCESS | Metrics & More | Article Recommendations | Supporting Information

ABSTRACT: As one of the most promising candidates of photoanode material, bismuth vanadate ($BiVO_4$) has been paid wide attention and achieved remarkable progress. However, the full exploitation of solar-energy-conversion potential of bismuth vanadate ($BiVO_4$) is still limited by poor charge transport. Introducing dopants into $BiVO_4$ has been proved to be a feasible method to improve the photoelectrochemical water splitting performance. In this work, lithium is introduced as an interstitial dopant to crystalline $BiVO_4$ thin film photoanode, with the aid of pulsed laser deposition (PLD). Solid-state transport characterization demonstrates increased carrier density and electron conductivity in $BiVO_4$ bulk due to interstitial lithium doping, which also increased the photocurrent and photon-to-current conversion efficiency both by up to 20% for solar water splitting. Computational results based on density functional theory determine the effect of lithium doping on the electronic and atomic structures of $BiVO_4$ and verify the role of lithium dopant as a shallow donor that improves the conductivity of $BiVO_4$.

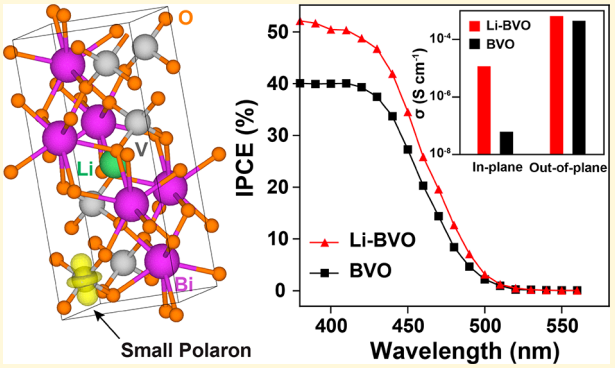

INTRODUCTION

Photoelectrochemical (PEC) solar fuel conversion offers an alternative and environmentally friendly approach to addressing the outlook of irreversible climate change in the near future, due to CO_2 emission from fossil fuel consumption.[1,2] The design and construction of efficient and robust photoelectrochemical cell devices, normally composed of semiconductor photoelectrodes, is the core of harvesting solar energy through photoelectrochemical solar water splitting.[3−5] Among various semiconductor photoelectrode materials, bismuth vanadate ($BiVO_4$) has emerged as one of the most promising photoanode candidates, because of its many outstanding advantages including a relatively narrow bandgap (2.4−2.6 eV), suitable band alignment to water redox reactions, favorable photocurrent onset, and reasonable stability in aqueous environment, etc.[6,7] However, its full potential for solar energy harvesting is currently hindered by several material limitations, such as low majority carrier (electron) mobility, mediocre electron−hole separation efficiency, and a high kinetic barrier for carrier injection across the aqueous interface.[8]

Doping with extrinsic defects is a viable strategy to enhance the photoelectrochemical performance of $BiVO_4$ photoanode by improving charge transport, separation, and/or light absorption.[9−11] As a ternary oxide, there are several kinds of sites available for bulk doping in $BiVO_4$, including substitutional doping at Bi-, V-, and O-sites, as well as interstitial doping sites.[4] The related literature of intrinsic/extrinsic defect doping in $BiVO_4$ is summarized in Table S1. To improve the majority carrier transport, the most common doping method is to use hexavalent Mo or W as V site substituent, which can significantly increase the major carrier density and improve the electron mobility by lowering the small polaron hopping barrier.[7,9,10,12] However, the V-site donors often contribute to hole traps and reduce the hole diffusion length, which limits the overall improvement to water splitting activity.[13] A few nonmetallic dopants have been applied to the O-site in $BiVO_4$ as well, including nitrogen,[11] fluorine,[14] and oxygen vacancy (V_O), which all demonstrate improvement to the photocatalytic performance at various degrees. In recent years, much interest has been received to investigate interstitial hydrogen as a donor defect in BVO, which is usually introduced through postsynthesis treatments such as thermal annealing in hydrogen.[15−17] Although clearly improving the conductivity and photocatalytic activity of BVO, such treatment would inevitably introduce extra oxygen vacancies to the lattice,

Received: April 6, 2020
Revised: July 13, 2020
Published: July 14, 2020

https://dx.doi.org/10.1021/acs.chemmater.0c01481
Chem. Mater. 2020, 32, 6401−6409

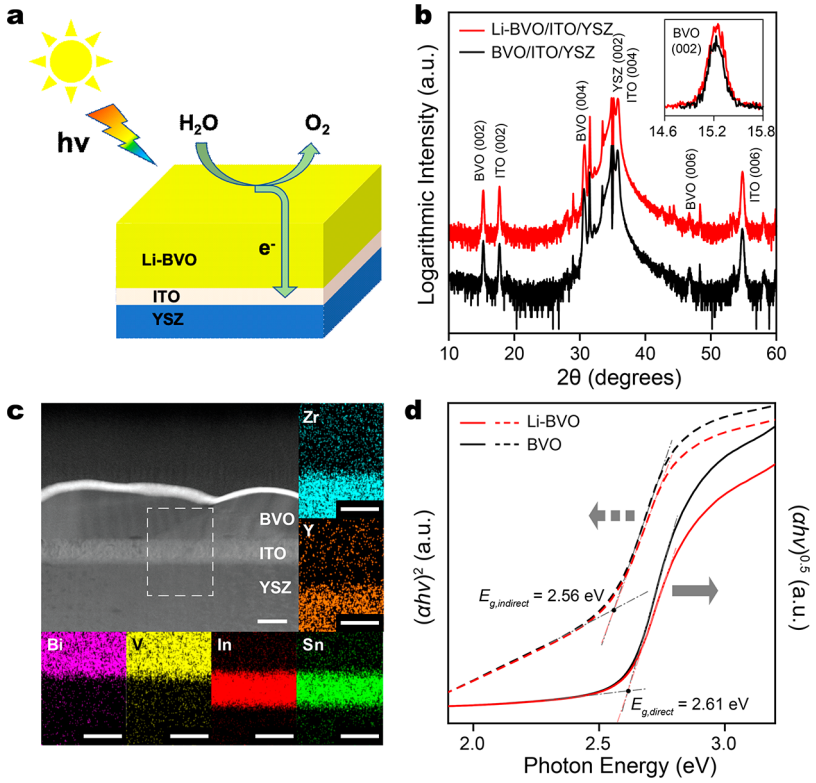

Figure 1. (a) Device layout of Li-doped BVO thin film photoanode. (b) X-ray diffraction (XRD) patterns of 5% Li-doped BVO (red) and pristine BVO (black) thin films. (inset) A zoomed-in view for the BVO(002) diffraction peaks of the two samples. (c) HAADF-STEM image of the cross-section of 5% Li-doped BVO/ITO/YSZ heterostructure (upper left) and EDX mapping for the area marked by the dashed rectangle. Scale bars = 100 nm. (d) Tauc plots of 5% Li-doped BVO (red) and pristine BVO (black) that represent direct transition (solid) and indirect transition (dashed).

which also act as donor defects and make it difficult to explicitly evaluate the role of interstitial hydrogen.

In recent years, $BiVO_4$ has been proposed as a promising anode material in Li-ion capacitors, due to its excellent volumetric capacity that benefited from the ion insertion/extraction process and energetically favorable lithiation.[18−20] Yin et al. reported that Li can serve as a shallow donor at the interstitial site in $BiVO_4$ from a computational perspective,[21] although this work did not consider the formation of small polarons and their role on carrier concentration and transport. Here we investigate the use of lithium, a group I metal that is earth abundant and isoelectronic to hydrogen, as an interstitial dopant in BVO, through a combined computational and experimental study. The small size of lithium (0.76 Å) as compared to the interstitial site (octahedral, 2.09 Å) determines the role of the interstitial dopant. On the basis of a synthetic strategy developed by our group in a series of previous work, Li-doped single-crystalline BVO thin film photoanodes are fabricated in a single step utilizing pulsed laser deposition (PLD),[8,22,23] which offers a facile and consistent way to tune the thin film stoichiometry by simply adjusting the elemental composition of laser ablation target within a similar range.[24] When compared to the photoanode of pristine BVO fabricated under identical conditions, the doping of Li leads to a 20% improvement in photocatalytic activity for water splitting that is accompanied by a significant increase of electrical conductivity. Computational studies by first-principles calculations confirm the stability of Li as an interstitial dopant and systematically determine the effect of Li-doping on the atomic and electronic structures, optical absorption spectra, and carrier transport properties, whereas the latter is largely defined by the hopping transport of small polarons near V^{5+} centers. The doping effect on polaron hopping in $BiVO_4$ has been investigated in several computational works,[10,11,25−27] by employing either a microscopic picture from polaron hopping rates with kinetic Monte Carlo sampling or a macroscopic picture of small polaron theory from the dielectric continuum model. In this work, we follow the macroscopic methodology to evaluate the effect of interstitial Li-dopant and conclude that doping has little effect on the small polaron mobility, despite introducing shallow donors and significantly increasing the majority carrier density. These computational results agree very well with experimental findings through solid-state transport measurements, which serve as an explicit confirmation to the effectiveness of interstitial doping of group I elements.

RESULTS AND DISCUSSION

Crystalline thin film photoanodes of pristine BVO and Li-doped BVO (Li-BVO) are fabricated over (001) yttrium-stabilized zirconia (YSZ) substrates by pulsed laser deposition (PLD) at conditions similar to those in our previous reports (Figure 1a).[8] Between the BVO layer and YSZ substrate, an epitaxial buffer layer of indium tin oxide (ITO) is grown by PLD as the conductive back contact.[8] In a typical photoanode, the BVO layer is 140 nm thick and the ITO layer is 50 nm. The doping levels of BVO thin films are regulated by the stoichiometry of laser ablation targets. To ensure Li being doped into interstitial sites, the Bi to V ratio is kept at unity for all targets, with various amounts of Li added in the form of

https://dx.doi.org/10.1021/acs.chemmater.0c01481
Chem. Mater. 2020, 32, 6401−6409

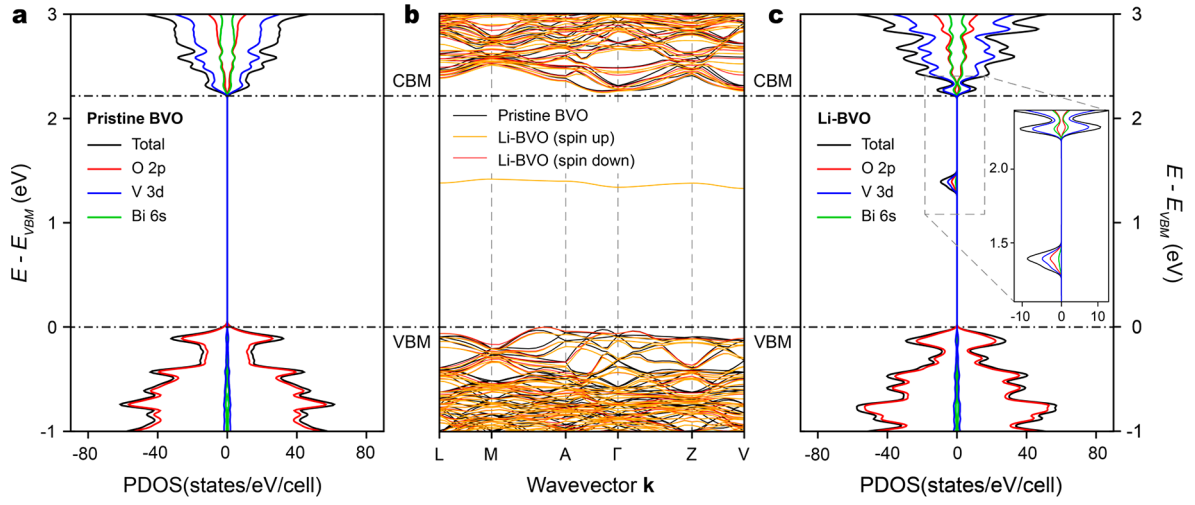

Figure 2. (a) Total (black) and projected (red for O 2p, blue for V 3d, and green for Bi 6s) density of states for pristine $BiVO_4$. (b) Band structures of pristine (black) and Li-doped (orange = spin up, red = spin down) $BiVO_4$. The VBM is set to zero in both cases. The occupied state around 1.4 eV corresponds to the electron polaron contributed by Li doping. (c) Total and projected density of states for Li-doped $BiVO_4$. (Inset) The polaron state induced by Li, which is mostly composed of V 3d and O 2p states. All three panels share the same energy scale on the *y*-axis.

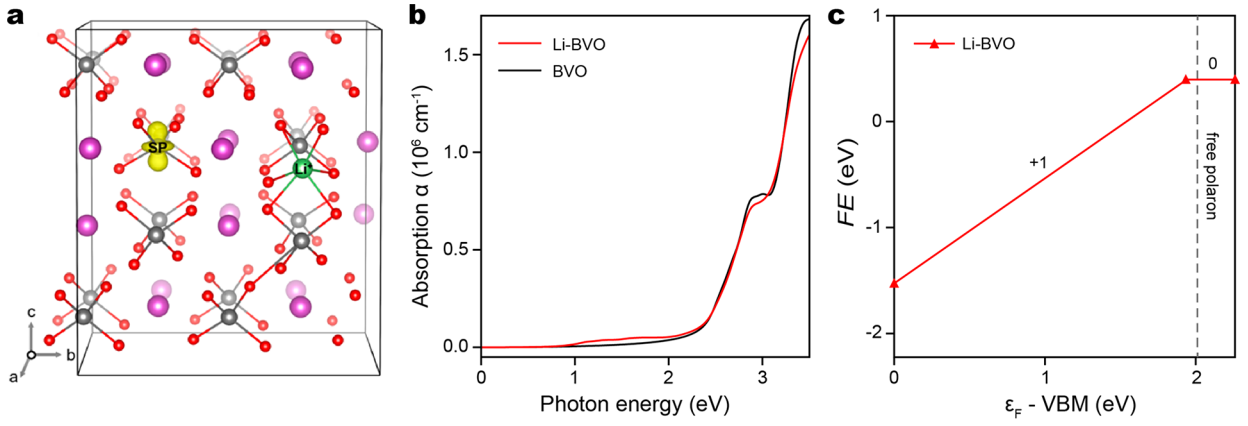

Figure 3. (a) Li-doped $BiVO_4$ (green for Li, purple for Bi, gray for V, and red for O), with isosurface shown for the electron small polaron (yellow cloud labeled "SP" on V atom). An isosurface value of 10% of the maximum is used. (b) Calculated absorption spectra of pristine (black) and Li-doped (red) $BiVO_4$. Li-doped $BiVO_4$ has a negligible change in band−band absorption above 2 eV and introduced transitions below 2 eV, due to polaron state-band transitions. (c) Defect formation energy (FE) diagram of Li in $BiVO_4$ computed at the O-poor condition. FE diagram for all possible p-type compensating defects for Li interstitial (n-type) can be found in Supporting Information, Figure S6.

Li_2CO_3, for Li doping levels of 0% (pristine), 5%, and 10%, in terms of atomic percentage (at. %) to $BiVO_4$ unit. The incorporation of lithium into the BVO thin film is confirmed by inductively coupled plasma mass spectrometry (ICP-MS), with the doping level identical to the target. In the discussion that follows, the Li-BVO film has a nominal Li doping level of 5 at. % unless otherwise specified. Scanning electron microscopy (SEM, Figure S1a,b) and atomic force microscopy (AFM, Figure S1c) reveal a grainy surface morphology with an RMS surface roughness of 19 ± 3 nm, which is similar between Li-doped and pristine BVO. X-ray diffraction (XRD) confirms that the Li-BVO film has high phase purity as monoclinic scheelite (space group *I*2/*b*, PDF no. 01-14-0688) and is epitaxial to the ITO/YSZ substrate, with only *c*-plane (00*l*) diffraction peaks of BVO presented (Figure 1b).[10] The XRD patterns of Li-BVO and pristine BVO are very similar to barely any peak shift (Figure 1b, inset), which indicates that Li interstitial has a negligible impact on the lattice parameters of BVO. This is likely due to the smaller size of lithium ion (0.76 Å) when compared to the interstitial site (octahedral, 2.09 Å).[28] The X-ray absorption near-edge structure (XANES) spectra collected at the V *K*-edge also show great similarity between Li-BVO and pristine BVO, which suggests that Li doping brings negligible structural distortion at the V^{5+} center (Figure S2). The phase purity of the Li-BVO/ITO/YSZ heterostructure is confirmed by high-angle annular dark-field scanning transmission electron microscopy (HAADF-STEM, Figure 1c).

X-ray photoelectron spectroscopy (XPS) verifies that Bi and V, respectively, have an oxidation state of +3 and +5 in both pristine and Li-doped BVO, despite a subtle difference in binding energy values (Figure S3). The binding energies are 163.90 eV (Bi $4f_{5/2}$), 158.55 eV (Bi $4f_{7/2}$), 524.05 eV (V $2p_{1/2}$), and 516.55 eV (V $2p_{3/2}$) for Li-BVO, which all shift toward lower energy by 0.5−0.6 eV when compared to pristine BVO. This confirms the role of Li as a donor defect to BVO lattice, which contributes extra electrons to the conduction band and lowers electron binding energies for each constituent. In addition, the content of oxygen vacancies near the sample surface is analyzed using an O 1s core-level XPS spectrum and

https://dx.doi.org/10.1021/acs.chemmater.0c01481
Chem. Mater. 2020, 32, 6401−6409

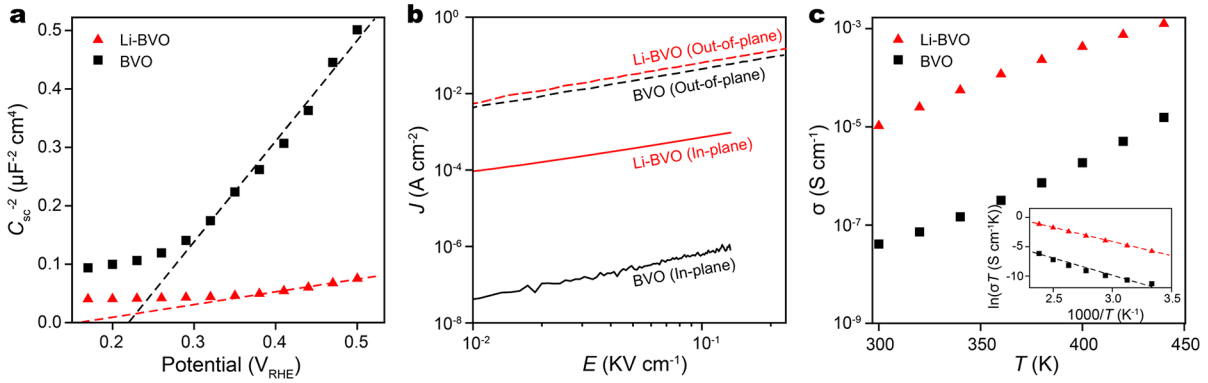

Figure 4. (a) Mott−Schottky plots of 5% Li-doped BVO (red) and pristine BVO (black). Their respective linear fittings are shown as the dashed lines. (b) Out-of-plane (dashed) and in-plane (solid) current−voltage (J−E) curves of 5% Li-doped BVO (red) and pristine BVO (black). (c) Temperature-dependent in-plane conductivity of 5% Li-doped BVO (red) and pristine BVO (black). The inset shows the respective linear fittings based on the small-polaron transport model.

shows barely any difference with or without Li doping (Figure S4).[29] Optical extinction spectra of pristine and Li-BVO are measured in the spectral range of 350−700 nm, by using an ITO/YSZ substrate as spectral reference. The spectral profile and optical densities are similar between Li-doped and pristine BVO (Figure S5). By using the Tauc plot,[30] we determine a direct band gap of 2.61 eV and an indirect band gap of 2.56 eV for Li-BVO, which are identical to those of pristine BVO and suggest a negligible impact to the optical band gap due to Li doping (Figure 1d).

First-principles calculations using the DFT+U method are performed for both Li-doped and pristine BVO. For Li-BVO, the calculations are performed with Li interstitial doping in a 96-atom supercell, that is, 1 Li:16 $BiVO_4$. The calculation on formation enthalpy confirms that Li stably occupies the interstitial site that is 6-coordinated with Li−O bond lengths between 2.04 and 2.26 Å as shown in Figure 3a. According to the calculated electronic band structure shown in Figure 2, the band gap of pristine BVO is 2.26 eV with an indirect transition, consistent with previous DFT+U calculations.[11,31] After Li doping, the band gap of BVO remains unchanged (without considering the isolated gap state) as shown in Figure 2b, which is comparable to the experimental finding. Li-doping introduces a localized midgap state (Figure 2b) that corresponds to the electron small polaron formed by the electron donated by Li with the local lattice distortion on a single V site (Figure 3a). To evaluate the effects of Li-doping on optical absorption, the complex dielectric function ($\tilde{\varepsilon} = \varepsilon_1 + i\varepsilon_2$) is computed using the random phase approximation as implemented in the YAMBO code[32] with eigenvalues and wave functions computed at the DFT+U level. The absorption coefficient $\alpha(\omega)$ is given by[33−35]

$$\alpha(\omega) = \frac{\omega}{c}\frac{\varepsilon_2(\omega)}{\sqrt{\frac{\varepsilon_1(\omega) + \sqrt{\varepsilon_1(\omega)^2 + \varepsilon_2(\omega)^2}}{2}}}$$

The calculated absorption spectrum (Figure 3b) shows a negligible change in the main absorption edge of BVO around 2.3 eV. However, Li-doping does introduce weak additional optical absorption below 2 eV, which must be due to transitions between the conduction band and the midgap electron polaron state, according to the electronic structure of Li-BVO.

The role of Li dopant as a donor defect is experimentally confirmed by electrochemical impedance spectroscopy (EIS) studies that determine space-charge capacitance (C_{sc}) at a series of potentials (E). The donor density (N_D) is then deduced using the Mott−Schottky model:

$$\frac{1}{C_{sc}^2} = \frac{2}{e\varepsilon\varepsilon_0 N_D}\left(E - E_{FB} - \frac{k_B T}{e}\right)$$

where e is the magnitude of elementary charge, $\varepsilon = 68$ is the relative permittivity of BVO, ε_0 is the vacuum permittivity, E_{FB} is the flat band potential, and $k_B T$ is the thermal energy. According to the Mott−Schottky (C_{sc}^{-2}−E) plot (Figure 4a), the Li-BVO photoanode is uniformly n-type doped with $N_D = 9.52 \times 10^{18}$ cm^{-3} and $E_{FB} = 0.16$ V_{RHE}. The donor density is 8 times higher than that of pristine $BiVO_4$ ($N_D = 1.20 \times 10^{18}$ cm^{-3}), which confirms the active role of Li as an n-type donor.[8] Had Li been substitutionally doped to replace Bi or V, the photoelectrode would exhibit a p-type doping rather than the observed n-type doping. Solid-state transport measurements reveal strong anisotropy in conductivity for both Li-doped and pristine BVO thin films, with significantly higher out-of-plane conductivity ($\sigma_\perp$) than in-plane conductivity ($\sigma_\parallel$). As explained in our previous work, this is due to the presence of vertical domain boundaries, which gives rise to an extra conductive channel for out-of-plane electronic transport.[8] Li doping increases the electronic conductivity of the BVO film, with the effect particularly significant for $\sigma_\parallel$ (Figure 4b). At room temperature, $\sigma_\parallel$ of Li-BVO is 1.16×10^{-5} S cm^{-1} and is over 2 orders of magnitude larger than that of pristine BVO (6.22×10^{-8} S cm^{-1}), which suggests that interstitial Li acts as a shallow donor. On the other hand, the out-of-plane conductivity of Li-BVO is only about 40% larger than that of pristine BVO (6.44×10^{-4} S cm^{-1} vs 4.48×10^{-4} S cm^{-1}), which matches the assertion that the out-of-plane charge transport is mostly contributed by domain boundaries rather than carriers in the bulk energy band. From room temperature to 450 K, the in-plane conductivity increases monotonically against temperature, for both Li-doped and pristine BVO (Figure 4c). The behavior is consistent with the small polaron hopping mechanism,[36−38] according to which a polaron hopping barrier, E_h, governs over the temperature dependence of conductivity, through the relation $\sigma(T) \propto T^{-1} \exp(-E_h/k_B T)$.[8,10] Linear fitting according to the relation suggests that, although Li-doping significantly increases carrier concentra-

https://dx.doi.org/10.1021/acs.chemmater.0c01481
Chem. Mater. 2020, 32, 6401−6409

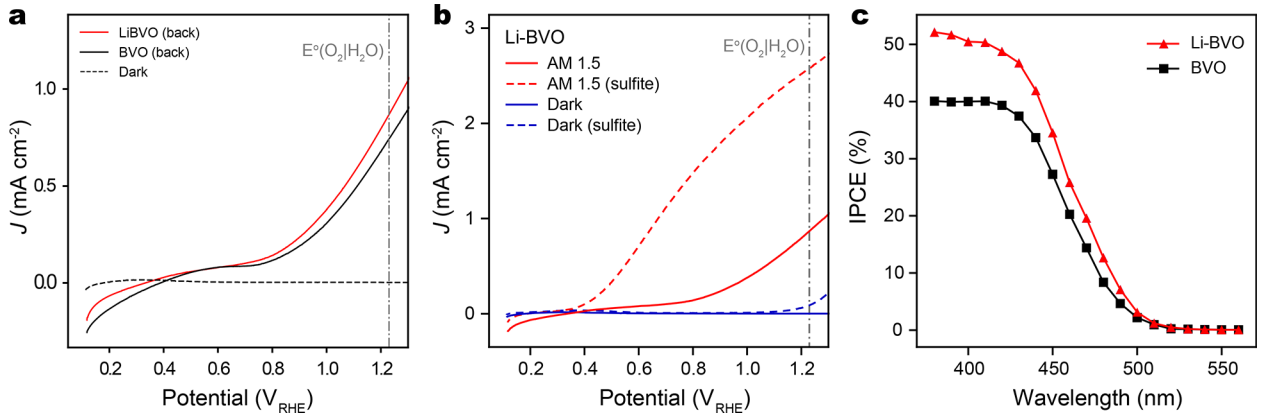

Figure 5. (a) Photocurrent density−potential characteristics (J−V curve) of 5% Li-doped BVO (red) and pristine BVO (black) in phosphate buffer (pH 7) under back illumination (solid). The dashed line represents the J−V curve of 5% Li-doped BVO in the dark. (b) Photocurrent density−potential characteristics (J−E curve) of 5% Li-doped BVO in phosphate buffer (pH 7) without (solid) and with (dashed) 1.0 M sulfite (Na_2SO_3) under AM 1.5 illumination (red) and in the dark (blue). (c) IPCE versus wavelength at 1.23 V_{RHE} of 5% Li-doped BVO (red) and pristine BVO (black) in phosphate buffer (pH 7) with 1.0 M sulfite (Na_2SO_3) under back illumination.

tion, its effect on hopping barrier is relatively small. As compared to pristine BVO (E_h = 462 meV), Li-doping only lowers the barrier by about 30 meV, to 431 meV (Figure 4c, inset).

First-principles calculations of the ionization energy of the electron polaron contributed by interstitial Li confirm it behaves as a shallow donor in BVO. To consider the effects of Li on the carrier concentration in BVO, it is necessary to compute the formation energy of the defect in each of its charge states q.

$$\mathrm{FE}_q[\varepsilon_F] = E_q - E_{pst} - \sum_i \mu_i \Delta N_i + q\varepsilon_F + \Delta_q$$

Here, FE_q is the formation energy of a defect with charge q, E_q is the total energy of the defect system (Li-doped BVO) with charge q, E_{pst} is the total energy of the pristine BVO, ΔN_i is the change in the number of atomic species i with chemical potential μ_i, ε_F is the Fermi energy, and Δ_q is the defect charge correction.[39] Given that BVO is deposited under a relatively low pressure of oxygen (20 mTorr) and n-type doped, the FE_q values are calculated at the O-poor condition (μ(O) = −2.8 eV), where Li interstitial has a lower formation energy than other possible point defects (Figure S6).[21] The value of the Fermi level (ε_F) in which the system undergoes a transition of charge state q to q' (specifically for interstitial Li, q = 1, q' = 0) defines the charge transition level $\varepsilon^{q|q'}$.

$$\varepsilon^{q|q'} = \frac{\mathrm{FE}_q[\varepsilon_F] - \mathrm{FE}_{q'}[\varepsilon_F]}{q' - q}$$

Typically, the charge transition level of an electron donor from one charge state to a more positive charge state referenced to the CBM defines the ionization energy of the defect, which is 0.319 eV for Li doping, and implies Li is rather difficult to be ionized at room temperature. However, due to the spontaneous formation of small polarons in BVO,[40] the feasibility of small polaron hopping is determined not by the ionization energy of the defect with respect to the CBM but by the ionization energy of the defect with respect to a free polaron state where the polaron is not bound to a defect.[27,34,41,42] Therefore, the true ionization energy of interstitial Li is equal to the energy difference between the charge transition levels of the defects (0.319 eV below CBM, solid red dots in Figure 3c) and the free polaron level (0.248 eV below CBM, gray dashed line in Figure 3c), that is, 0.071 eV, relatively small as compared to kT. The Fermi level corresponding to the $\varepsilon^{0|-1}$ transition in the pristine system defines the free polaron level. Therefore, interstitial Li contributes electrons to the system without introducing trap states and thus increases the majority carrier concentration of BVO.

Computation based on the small polaron theory reveals that Li-doping barely affects the majority carrier mobility in BVO. Here, the small polaron binding energy (W_P) and activation energy (W_H) are calculated using the phonon frequencies and dielectric constants from density functional perturbation theory, described in detail in the Supporting Information.[43] According to the results, the small polaron binding energy W_P is over 0.5 eV (Table S2) and is significantly larger than k_BT at room temperature (26 meV), which confirms the energetically favorable formation of small polarons and the polaronic nature of BVO. On the other hand, Li-doping only slightly weakens the BVO lattice and introduces minor changes to the static and high-frequency dielectric constants (ε_0 and ε_∞). Given that $W_H \propto (\varepsilon_\infty^{-1} - \varepsilon_0^{-1})$, the value of W_H turns out to be identical between Li-doped and pristine BVO (0.152 eV, Table S2). Because the carrier mobility $\mu \propto T^{-1} \exp(-W_H/k_BT)$, we further conclude that Li-doping does not affect the mobility of BVO, and that the improved conductivity observed experimentally is the sole result of increased carrier concentration.

Improved electron conductivity in Li-BVO leads to enhanced photocatalytic activity. The photoelectrochemical characteristics of Li-BVO thin film photoanodes are studied by linear sweep voltammetry under simulated AM 1.5G radiation and are compared to those of pristine BVO. The illumination is from the back side of photoanode to compensate the low electron mobility of BVO. A phosphate buffer at pH 7 is used as the electrolyte to measure water oxidation efficiency. For BVO photoanodes of different Li doping levels, the photocurrent reaches a maximum when n_{Li}/n_{BVO} = 0.05, that is, a doping level of 5 at. % (Figure S7). According to the photocurrent density−potential (J−V) relations in Figure 5a, water oxidation over the Li-BVO photoanode reaches a photocurrent density (J^{aq}) of 0.87 mA/cm^2 at 1.23 V_{RHE}, which is 18% larger than the pristine BVO (0.74 mA/cm^2)

https://dx.doi.org/10.1021/acs.chemmater.0c01481
Chem. Mater. 2020, 32, 6401−6409

under identical conditions. The relatively low photocurrents reflect the low activity of BVO surface for water oxidation. To isolate the effect of Li-doping on charge carrier separation, 1.0 M sodium sulfite (Na_2SO_3) is added as a hole scavenger to eliminate the surface kinetic barrier. Accordingly, photocurrent densities in buffered sulfite electrolyte increase significantly for both samples, with a cathodic shift of the photocurrent onset potential by about 0.2 V (Figure 5b). The photocurrent from Li-BVO reaches 2.57 mA/cm^2, which is 20% higher than that of pristine BVO (2.15 mA/cm^2, Figure S8). The enhancement to photocurrent is apparently correlated to the improvement in majority carrier (electron) transport led by Li-doping. On the other hand, the PEC activity is reduced if the doping level is further elevated to 10% (Figure S7), due to the increased impact of minority carrier recombination at donor sites. Li doping also induces a relatively small cathodic shift to the onset potential for water oxidation. However, due to its very slow kinetics near the flat band potential, the exact shift cannot be determined very precisely. We note the enhancement to the photocatalytic activity and electron conductivity is similar to the case of BVO photoanode post-treated by thermal annealing in hydrogen (H-BVO).[16] However, both H-interstitial and oxygen vacancies may be introduced in the case of H-BVO, which make it less straightforward to determine the contribution of interstitial site doping. In the present case of Li-BVO, the fabrication process does not introduce extra oxygen vacancies when compared to pristine BVO, which explicitly demonstrates the effectiveness of doping BVO with a group I element at the interstitial site as a shallow donor.

Photocurrent delivered by a photoelectrode is limited by the charge separation efficiency (η_{sep}) and carrier injection efficiency into the electrolyte (η_{inj}), that is, $J = J_{max}\eta_{sep}\eta_{inj}$, in which J_{max} is the theoretical maximum photocurrent density derived from the AM 1.5G spectrum and optical absorption profile of the photoanode. For a 140 nm-thick BVO film, we find J_{max} = 4.85 mA/cm^2. By assuming η_{inj} = 1 in sulfite electrolyte, we determine η_{sep} = 0.53 for Li-BVO, which is 20% higher than that of pristine BVO (η_{sep} = 0.44). The result is consistent with the measurement of incident photon to current efficiency (IPCE, Figure 5c), in which a uniform improvement in IPCE values is achieved by Li-doping, for all energies above BVO band gap. We note that, although doping with donors is a proven strategy to improve electron transport in the BVO water splitting photoanode, such a strategy usually improves η_{sep} only at low doping levels (≤2%), as the donor defects such as Mo^{VI} also serve as a hole trap. However, in the present case, the optimal Li doping level is as high as 5 at. %, which suggests that interstitial Li dopant is a less effective hole trap. This may be due to the smaller size (0.76 Å) and low charge (+1) of Li^+. On the other hand, the hole injection efficiency into water, η_{inj}^{aq}, is conveniently given by $\eta_{inj}^{aq} = J^{aq}/J^{sulfite}$. We therefore determine that η_{inj}^{aq} equals 34% for both Li-doped and pristine BVO. The values are very similar, which suggests that Li-doping has little effect on BVO surface. The summary of photocurrents in phosphate buffer (pH 7) with and without 1.0 M sulfite (Na_2SO_3) and calculated charge injection and separation efficiency of Li-BVO and pristine BVO is shown in Table 1. In our previous works, we used a similar fabrication method to introduce dopants such as Mo[10] and used the postgrowth treatment, such as CO-reduction, to introduce oxygen vacancies.[13] The photocurrent from Li-BVO is nearly 10% higher than that from Mo-doped BVO and is very comparable with CO-treated BVO that contains oxygen vacancy defects. The simple, one-step fabrication discussed here makes Li doping a competitive option of doping for BVO photoanodes.

Table 1. Summary of Photocurrents in Phosphate Buffer (pH 7) with ($J_{sulfite}$) and without (J_{water}) 1.0 M Sulfite (Na_2SO_3) and the Calculated Charge Injection and Separation Efficiency of 5% Li-Doped BVO and Pristine BVO

	$J_{sulfite}$ (mA/cm^2)	J_{water} (mA/cm^2)	η_{inj} (%)	η_{sep} (%)
5% Li-doped BVO	2.57	0.87	34	53
pristine BVO	2.15	0.74	34	44

In summary, lithium is investigated and identified as a unique interstitial dopant in bismuth vanadate that boosts its photoelectrochemical water oxidation performance, based on the computational and experimental studies on single-crystalline bismuth vanadate thin film. With doping concentration optimized at 5 at. %, Li-BVO increases the photoelectrochemical water oxidation activity by about 20%, when compared to the pristine BVO thin film of identical morphology and crystalline phase. First-principles calculations suggest that interstitial Li acts as a shallow electron donor in BVO and significantly improves the majority carrier concentration, without a significant change to the carrier mobility. These findings are confirmed experimentally by electrochemical impedance spectroscopy and solid-state transport measurement, in which we observe an increase of conductivity by almost 2 orders of magnitude. Because the fabrication process introduces no extra oxygen vacancies, we thus obtain explicit confirmation that interstitial Li dopant is indeed an effective electron donor in BVO. As such, this work casts new insight into using group I elements as a low cost, environmentally friendly dopant to improve electronic transport in metal oxide-based solar water splitting photoelectrodes.

METHODS

Computational Methods. Spin-polarized DFT+U calculations are carried out using the open-source plane-wave code Quantum-ESPRESSO[44] with norm-conserving pseudopotentials[45] and the Perdew−Burke−Ernzerhof exchange correlation functional.[46] A Hubbard U correction of 2.7 eV is applied on all vanadium atoms in accordance with ref 47. All calculations are performed with a 96-atom supercell, unless otherwise noted. A 2 × 2 × 2 k-point mesh is used for Brillouin-zone sampling, with a wave function energy cutoff of 50 Ry and a charge density cutoff of 300 Ry. The lattice parameters are optimized for the pristine $BiVO_4$ cell, and then held constant for the doped cells. For charged systems, a charged cell correction is implemented to minimize the effects of spurious charge interactions between periodic images.[39] All phonon and dielectric constant calculations are performed with the Vienna ab initio software package (VASP)[48] with projector augmented-wave (PAW) potentials[49] and a PBE+U exchange correlation functional. These calculations used a 48-atom supercell with a 3 × 3 × 2 k-point mesh with a wave function energy cutoff of 520 eV.

Thin Film Photoanode Preparation. Li-doped and pristine BVO thin films are deposited on YSZ(001) single-crystalline substrates (MTI Corp) by PLD using a KrF excimer laser (λ = 248 nm) that operated at a repetition rate of 20 Hz and a fluence of 1.8 J/cm^2. Li-doped and pristine BVO laser ablation targets are prepared by a conventional ceramic sintering method, using $BiVO_4$ powder, with and without the addition of Li_2CO_3 powder. For photoelectrochemical characterization of BVO photoanodes, a 50 nm thick ITO film is first deposited over the YSZ substrate at 600 °C and under a base pressure of 6 × 10^{-7} Torr. BVO films are subsequently deposited at

https://dx.doi.org/10.1021/acs.chemmater.0c01481
Chem. Mater. 2020, 32, 6401−6409

625 °C in 20 mTorr of oxygen. After deposition, the films are cooled to room temperature under the same atmosphere at a rate of 10 °C min^{-1}.

Microstructural, Chemical, and Optical Characterization. Crystalline phases of the thin film are characterized by X-ray diffraction (XRD, Rigaku Ultima III) using Cu Kα radiation (λ = 1.5418 Å). The surface morphology is investigated with the aid of scanning electron microscopy (SEM, Hitachi 4800) and atomic force microscopy (AFM, Park NX 20). The microstructure of the film is characterized by transmission electron microscopy (TEM, FEI Talos 200X). The optical absorption and bandgap of the thin film are obtained from a UV−vis−NIR spectrophotometer (PerkinElmer, Lambda 950, and Lambda 25). X-ray photoelectron spectroscopy measurement is performed in a high vacuum (~10^{-7} Torr) using Al Kα (1486.6 eV) as the excitation source.

Electronic Transport Characterization. Electrochemical impedance spectroscopy (EIS) is carried out in a pH 7.0 phosphate buffer, in a frequency range between 100 Hz and 100 kHz. The measured spectra are analyzed by Zview software (Scribner Associates). Solid-state electronic transport properties are characterized using a probe station (Signatone), with Ti (3 nm)/Au (60 nm) top electrodes deposited over the BVO thin film by thermal evaporation. For out-of-plane measurements, the ITO underlayer is partially exposed by using a shadow mask during BVO deposition, so that the measurements are between the top Ti/Au electrode and the bottom ITO electrode. For in-plane measurements, BVO thin films are deposited over bare YSZ substrate without the ITO underlayer, and the measurements are between the pairs of top electrodes.

Photoelectrochemical Characterization. PEC characterization is performed using a potentiostat (PAR VersaStat 4) in the three-electrode configuration, with a Li-doped or pristine BVO thin film as the working electrode, Ag/AgCl (3 M KCl) as the reference electrode, and a Pt wire as the counter electrode. The electrolyte solution is a pH phosphate buffer, with or without the addition of 1.0 M Na_2SO_3 as hole scavenger. Solar illumination is simulated by a 150 W solar simulator with an AM 1.5G filter (Newport). The incident light power is calibrated by a calibrated quartz-windowed Si solar cell (Newport) to a nominal power of 100 mW cm^{-2}. For the incident photon-to-current efficiency (IPCE) measurement, monochromatized illumination is generated using a 300 W xenon arc lamp and a grating monochromator equipped with band-pass filters for removing higher order diffractions. The light power at each wavelength is measured by an optical power meter (Newport 1936-R) and a UV-enhanced Si photodiode sensor.

■ ASSOCIATED CONTENT

Supporting Information

The Supporting Information is available free of charge at https://pubs.acs.org/doi/10.1021/acs.chemmater.0c01481.

Calculation for carrier mobility based on small polaron hopping model, table of literature summary, SEM and AFM images, XPS spectra, XANES spectrum, UV−vis transmittance spectrum, Mott−Schottky plot, defect formation energy diagram, $J-V$ curves of doped BVO at different doping levels of lithium, and $J-V$ curves in phosphate buffer (pH 7) with 1.0 M sulfite (Na_2SO_3) (PDF)

■ AUTHOR INFORMATION

Corresponding Authors

Yuan Ping − *Department of Chemistry and Biochemistry, University of California, Santa Cruz, California 95064, United States;* orcid.org/0000-0002-0123-3389; Email: yuanping@uscs.edu

Mingzhao Liu − *Center for Functional Nanomaterials, Brookhaven National Laboratory, Upton, New York 11973, United States;* orcid.org/0000-0002-0999-5214; Email: mzliu@bnl.gov

Authors

Chenyu Zhou − *Center for Functional Nanomaterials, Brookhaven National Laboratory, Upton, New York 11973, United States; Department of Materials Science and Chemical Engineering, Stony Brook University, Stony Brook, New York 11794, United States;* orcid.org/0000-0002-2749-4739

Zachary Sanders-Bellis − *Department of Chemistry and Biochemistry, University of California, Santa Cruz, California 95064, United States*

Tyler J. Smart − *Department of Physics, University of California, Santa Cruz, California 95064, United States*

Wenrui Zhang − *Center for Functional Nanomaterials, Brookhaven National Laboratory, Upton, New York 11973, United States;* orcid.org/0000-0002-0223-1924

Lihua Zhang − *Center for Functional Nanomaterials, Brookhaven National Laboratory, Upton, New York 11973, United States*

Complete contact information is available at: https://pubs.acs.org/10.1021/acs.chemmater.0c01481

Notes

The authors declare no competing financial interest.

■ ACKNOWLEDGMENTS

This research used resources of the Center for Functional Nanomaterials and the Inner Shell Spectroscopy (8-ID) beamline of the National Synchrotron Light Source II, which are U.S. DOE Office of Science User Facilities, and the Scientific Data and Computing Center, a component of the Computational Science Initiative, at Brookhaven National Laboratory under contract no. DE-SC0012704. Y.P. acknowledges financial support from the National Science Foundation under grant no. CHE-1904547. Y.P. also used the lux supercomputer at UC Santa Cruz, funded by NSF MRI grant AST 1828315, and the Extreme Science and Engineering Discovery Environment (XSEDE), which is supported by the National Science Foundation under grant number ACI1548562.

■ REFERENCES

(1) Walter, M. G.; Warren, E. L.; McKone, J. R.; Boettcher, S. W.; Mi, Q.; Santori, E. A.; Lewis, N. S. Solar Water Splitting Cells. *Chem. Rev.* **2010**, *110*, 6446−6473.

(2) Kang, D.; Kim, T. W.; Kubota, S. R.; Cardiel, A. C.; Cha, H. G.; Choi, K.-S. Electrochemical Synthesis of Photoelectrodes and Catalysts for Use in Solar Water Splitting. *Chem. Rev.* **2015**, *115*, 12839−12887.

(3) Sivula, K.; van de Krol, R. Semiconducting Materials for Photoelectrochemical Energy Conversion. *Nature Rev. Mater.* **2016**, *1*, 15010.

(4) Zhang, W.; Liu, M. Modulating Carrier Transport Via Defect Engineering in Solar Water Splitting Devices. *ACS Energy Lett.* **2019**, *4*, 834−843.

(5) Ager, J. W.; Shaner, M. R.; Walczak, K. A.; Sharp, I. D.; Ardo, S. Experimental Demonstrations of Spontaneous, Solar-Driven Photoelectrochemical Water Splitting. *Energy Environ. Sci.* **2015**, *8*, 2811−2824.

(6) Park, Y.; McDonald, K. J.; Choi, K.-S. Progress in Bismuth Vanadate Photoanodes for Use in Solar Water Oxidation. *Chem. Soc. Rev.* **2013**, *42*, 2321−2337.

(7) Lee, D. K.; Lee, D.; Lumley, M. A.; Choi, K.-S. Progress on Ternary Oxide-Based Photoanodes for Use in Photoelectrochemical Cells for Solar Water Splitting. *Chem. Soc. Rev.* **2019**, *48*, 2126−2157.
(8) Zhang, W.; Yan, D.; Li, J.; Wu, Q.; Cen, J.; Zhang, L.; Orlov, A.; Xin, H.; Tao, J.; Liu, M. Anomalous Conductivity Tailored by Domain-Boundary Transport in Crystalline Bismuth Vanadate Photoanodes. *Chem. Mater.* **2018**, *30*, 1677−1685.
(9) Rohloff, M.; Anke, B.; Zhang, S.; Gernert, U.; Scheu, C.; Lerch, M.; Fischer, A. Mo-Doped $BiVO_4$ Thin Films - High Photoelectrochemical Water Splitting Performance Achieved by a Tailored Structure and Morphology. *Sustain. Energy Fuels* **2017**, *1*, 1830−1846.
(10) Zhang, W.; Wu, F.; Li, J.; Yan, D.; Tao, J.; Ping, Y.; Liu, M. Unconventional Relation between Charge Transport and Photocurrent Via Boosting Small Polaron Hopping for Photoelectrochemical Water Splitting. *ACS Energy Lett.* **2018**, *3*, 2232−2239.
(11) Kim, T.; Ping, Y.; Galli, G.; Choi, K.-S. Simultaneous Enhancements in Photon Absorption and Charge Transport of Bismuth Vanadate Photoanodes for Solar Water Splitting. *Nat. Commun.* **2015**, *6*, 8769.
(12) Chen, L.; Toma, F. M.; Cooper, J. K.; Lyon, A.; Lin, Y.; Sharp, I. D.; Ager, J. W. Mo-Doped $BiVO_4$ Photoanodes Synthesized by Reactive Sputtering. *ChemSusChem* **2015**, *8*, 1066−1071.
(13) Zhang, W.; Song, L.; Cen, J.; Liu, M. Mechanistic Insights into Defect-Assisted Carrier Transport in Bismuth Vanadate Photoanodes. *J. Phys. Chem. C* **2019**, *123*, 20730−20736.
(14) Jiang, H.; Dai, H.; Deng, J.; Liu, Y.; Zhang, L.; Ji, K. Porous F-Doped $BiVO_4$: Synthesis and Enhanced Photocatalytic Performance for the Degradation of Phenol under Visible-Light Illumination. *Solid State Sci.* **2013**, *17*, 21−27.
(15) Newhouse, P. F.; Guevarra, D.; Umehara, M.; Boyd, D. A.; Zhou, L.; Cooper, J. K.; Haber, J. A.; Gregoire, J. M. Multi-Modal Optimization of Bismuth Vanadate Photoanodes Via Combinatorial Alloying and Hydrogen Processing. *Chem. Commun.* **2019**, *55*, 489−492.
(16) Jang, J. W.; Friedrich, D.; Muller, S.; Lamers, M.; Hempel, H.; Lardhi, S.; Cao, Z.; Harb, M.; Cavallo, L.; Heller, R.; Eichberger, R.; van de Krol, R.; Abdi, F. F. Enhancing Charge Carrier Lifetime in Metal Oxide Photoelectrodes through Mild Hydrogen Treatment. *Adv. Energy Mater.* **2017**, *7*, 1701536.
(17) Cooper, J. K.; Scott, S. B.; Ling, Y.; Yang, J.; Hao, S.; Li, Y.; Toma, F. M.; Stutzmann, M.; Lakshmi, K. V.; Sharp, I. D. Role of Hydrogen in Defining the N-Type Character of $BiVO_4$ Photoanodes. *Chem. Mater.* **2016**, *28*, 5761−5771.
(18) Dubal, D. P.; Jayaramulu, K.; Zboril, R.; Fischer, R. A.; Gomez-Romero, P. Unveiling $BiVO_4$ Nanorods as a Novel Anode Material for High Performance Lithium Ion Capacitors: Beyond Intercalation Strategies. *J. Mater. Chem. A* **2018**, *6*, 6096−6106.
(19) Dubal, D. P.; Patil, D. R.; Patil, S. S.; Munirathnam, N. R.; Gomez-Romero, P. $BiVO_4$ Fern Architectures: A Competitive Anode for Lithium-Ion Batteries. *ChemSusChem* **2017**, *10*, 4163−4169.
(20) Ruud, A.; Sottmann, J.; Vajeeston, P.; Fjellvag, H. Operando Investigations of Lithiation and Delithiation Processes in a $BiVO_4$ Anode Material. *Phys. Chem. Chem. Phys.* **2018**, *20*, 29798−29803.
(21) Yin, W. J.; Wei, S. H.; Al-Jassim, M. M.; Turner, J.; Yan, Y. Doping Properties of Monoclinic $BiVO_4$ Studied by First-Principles Density-Functional Theory. *Phys. Rev. B: Condens. Matter Mater. Phys.* **2011**, *83*, 155102.
(22) Jeong, S. Y.; Choi, K. S.; Shin, H. M.; Kim, T. L.; Song, J.; Yoon, S.; Jang, H. W.; Yoon, M. H.; Jeon, C.; Lee, J.; Lee, S. Enhanced Photocatalytic Performance Depending on Morphology of Bismuth Vanadate Thin Film Synthesized by Pulsed Laser Deposition. *ACS Appl. Mater. Interfaces* **2017**, *9*, 505−512.
(23) Rettie, A. J. E.; Mozaffari, S.; McDaniel, M. D.; Pearson, K. N.; Ekerdt, J. G.; Markert, J. T.; Mullins, C. B. Pulsed Laser Deposition of Epitaxial and Polycrystalline Bismuth Vanadate Thin Films. *J. Phys. Chem. C* **2014**, *118*, 26543−26550.
(24) Schou, J. Physical Aspects of the Pulsed Laser Deposition Technique: The Stoichiometric Transfer of Material from Target to Film. *Appl. Surf. Sci.* **2009**, *255*, 5191−5198.
(25) Smart, T. J.; Cardiel, A.; Wu, F.; Choi, K.-S.; Ping, Y. Mechanistic Insights of Enhanced Spin Polaron Conduction in Cuo through Atomic Doping. *npj Computational Materials* **2018**, *4*, 61.
(26) Wu, F.; Ping, Y. Combining Landau-Zener Theory and Kinetic Monet Carlo Sampling for Small Polaron Mobility of Doped $BiVO_4$ from First-Principles. *J. Mater. Chem. A* **2018**, *6*, 20025.
(27) Smart, T. J.; Ping, Y. Effect of Defects on the Small Polaron Formation and Transport Properties of Hematite from First-Principles Calculations. *J. Phys.: Condens. Matter* **2017**, *29*, 394006.
(28) Sun, Z.; Liu, G.; Fu, Z.; Hao, Z.; Zhang, J.; Novel Upconversion, A. Luminescent Material: Li^+ - or Mg^{2+}-Codoped $Bi_{3.84}W_{0.16}O_{6.24}$: Tm^{3+}, Yb^{3+} Phosphors and Their Temperature Sensing Properties. *Dyes Pigm.* **2018**, *151*, 287−295.
(29) Wang, S.; Chen, P.; Bai, Y.; Yun, J. H.; Liu, G.; Wang, L. New $BiVO_4$ Dual Photoanodes with Enriched Oxygen Vacancies for Efficient Solar-Driven Water Splitting. *Adv. Mater.* **2018**, *30*, 1800486.
(30) Tauc, J.; Grigorovici, R.; Vancu, A. Optical Properties and Electronic Structure of Amorphous Germanium. *Phys. Status Solidi B* **1966**, *15*, 627−637.
(31) Park, H.; Kweon, K.; Ye, H.; Paek, E.; Hwang, G.; Bard, A. Factors in the Metal Doping of $BiVO_4$ for Improved Photoelectrocatalytic Activity as Studied by Scanning Electrochemical Microscopy and First-Principles Density-Functional Calculation. *J. Phys. Chem. C* **2011**, *115*, 17870−17879.
(32) Marini, A.; Hogan, C.; Gruning, M.; Varsano, D. Yambo: An Ab Initio Tool for Excited State Calculations. *Comput. Phys. Commun.* **2009**, *180*, 1392−1403.
(33) Smart, T. J.; Pham, T. A.; Ping, Y.; Ogitsu, T. Optical Absorption Induced by Small Polaron Formation in Transition Metal Oxides: the Case of Co_3O_4. *Phys. Rev. Mater.* **2019**, *3*, 102401.
(34) Wheeler, G. P.; Baltazar, V. U.; Smart, T. J.; Radmilovic, A.; Ping, Y.; Choi, K.-S. Combined Theoretical and Experimental Investigations of Atomic Doping to Enhance Photon Absorption and Carrier Transport of $LaFeO_3$ Photocathodes. *Chem. Mater.* **2019**, *31*, 5890−5899.
(35) Ping, Y.; Rocca, D.; Galli, G. Optical Properties of Tungsten Trioxide from First-Principles Calculations. *Phys. Rev. B: Condens. Matter Mater. Phys.* **2013**, *87*, 165203.
(36) Austin, I. G.; Mott, N. F. Polarons in Crystalline and Non-Crystalline Materials. *Adv. Phys.* **1969**, *18*, 41−102.
(37) Rettie, A. J. E.; Chemelewski, W. D.; Emin, D.; Mullins, C. B. Unravelling Small-Polaron Transport in Metal Oxide Photoelectrodes. *J. Phys. Chem. Lett.* **2016**, *7*, 471−479.
(38) Ziwritsch, M.; Muller, S.; Hempel, H.; Unold, T.; Abdi, F. F.; van de Krol, R.; Friedrich, D.; Eichberger, R. Direct Time-Resolved Observation of Carrier Trapping and Polaron Conductivity in $BiVO_4$. *ACS Energy Lett.* **2016**, *1*, 888−894.
(39) Sundararaman, R.; Ping, Y. First-Principles Electrostatic Potentials for Reliable Alignment at Interfaces and Defects. *J. Chem. Phys.* **2017**, *146*, 104109.
(40) Rettie, A.; Lee, H.; Marshall, L.; Lin, J.; Capan, C.; Lindemuth, J.; McCloy, J.; Zhou, J.; Bard, A.; Mullins, C. Combined Charge Carrier Transport and Photoelectrochemical Characterization of $BiVO_4$ Single Crystals: Intrinsic Behavior of a Complex Metal Oxide. *J. Am. Chem. Soc.* **2013**, *135*, 11389−11396.
(41) Seo, H.; Ping, Y.; Galli, G. Role of Point Defects in Enhancing the Conductivity of $BiVO_4$. *Chem. Mater.* **2018**, *30*, 7793−7802.
(42) Radmilovic, A.; Smart, T. J.; Ping, Y.; Choi, K. S. Combined Experimental and Theoretical Investigations of n-Type $BiFeO_3$ for Use as a Photoanode in a Photoelectrochemical Cell. *Chem. Mater.* **2020**, *32*, 3262−3270.
(43) Baroni, S.; Gironcoli, S. d.; Corso, A. D.; Giannozzi, P. Phonons and Related Crystal Properties from Density-Functional Perturbation Theory. *Rev. Mod. Phys.* **2001**, *73*, 515−562.
(44) Giannozzi, P.; Baroni, S.; Bonini, N.; Calandra, M.; Car, R.; Cavazzoni, C.; Ceresoli, D.; Chiarotti, G. L.; Cococcioni, M.; Dabo, I.; Dal Corso, A.; de Gironcoli, S.; Fabris, S.; Fratesi, G.; Gebauer, R.; Gerstmann, U.; Gougoussis, C.; Kokalj, A.; Lazzeri, M.; Martin-Samos, L.; Marzari, N.; Mauri, F.; Mazzarello, R.; Paolini, S.;

https://dx.doi.org/10.1021/acs.chemmater.0c01481
Chem. Mater. 2020, 32, 6401−6409

Pasquarello, A.; Paulatto, L.; Sbraccia, C.; Scandolo, S.; Sclauzero, G.; Seitsonen, A. P.; Smogunov, A.; Umari, P.; Wentzcovitch, R. M. Quantum Espresso: A Modular and Open-Source Software Project for Quantum Simulations of Materials. *J. Phys.: Condens. Matter* **2009**, *21*, 19.

(45) Schlipf, M.; Gygi, F. Optimization Algorithm for the Generation of Oncv Pseudopotentials. *Comput. Phys. Commun.* **2015**, *196*, 36−44.

(46) Perdew, J.; Burke, K.; Ernzerhof, M. Generalized Gradient Approximation Made Simple. *Phys. Rev. Lett.* **1996**, *77*, 3865−3868.

(47) Park, H. S.; Kweon, K. E.; Ye, H.; Paek, E.; Hwang, G. S.; Bard, A. J. Factors in the Metal Doping of $BiVO_4$ for Improved Photoelectrocatalytic Activity as Studied by Scanning Electrochemical Microscopy and First-Principles Density-Functional Calculation. *J. Phys. Chem. C* **2011**, *115*, 17870−17879.

(48) Kresse, G.; Furthmuller, J. Efficient Iterative Schemes for Ab Initio Total-Energy Calculations Using a Plane-Wave Basis Set. *Phys. Rev. B: Condens. Matter Mater. Phys.* **1996**, *54*, 11169−11186.

(49) Blochl, P. E. Projector Augmented-Wave Method. *Phys. Rev. B: Condens. Matter Mater. Phys.* **1994**, *50*, 17953−17979.

https://dx.doi.org/10.1021/acs.chemmater.0c01481
Chem. Mater. 2020, 32, 6401−6409